Impact of Contact Resistance on the f_T and $f_{\max}$ of Graphene Versus MoS_2 Transistors

Kyle D. Holland, *Member, IEEE*, Ahsan U. Alam, Navid Paydavosi, Michael Wong, Christopher M. Rogers, Shahriar Rizwan, Diego Kienle, and Mani Vaidyanathan, *Member, IEEE*

***Abstract*—A key challenge in making 2-D materials viable for electronics is reducing the contact resistance ρ_C of the source and drain, which can otherwise severely curtail performance. We consider the impact of contact resistance on the performance of transistors made with single-layer graphene and MoS_2, two of the most popular 2-D materials presently under consideration for radio-frequency (RF) applications. While our focus is on the impact of ρ_C, we include the impact of all the device parasitics. We consider a device structure based on the 7-nm node of the ITRS and use the unity-current-gain and unity-power-gain frequencies (f_T and $f_{\max}$) found from quantum-mechanical simulations, ballistic for graphene and with scattering for MoS_2, as indicators of RF performance. We quantify our results in terms of the values of ρ_C needed to reach specific values of f_T and $f_{\max}$. In terms of peak performance (over all bias conditions), we show that graphene retains a significant edge over MoS_2, despite graphene's poor output conductance, with MoS_2 only being able to bridge the gap if considerably better contact resistances can be realized. However, with the bias current restricted to a technologically relevant value, we show that graphene loses much of its advantage, primarily due to a reduction in its transconductance g_m, and we show that MoS_2 can then meet or exceed the performance of graphene via the realization of contact resistances already achieved in multilayer structures. Our values of f_T for short-channel devices (around the 7-nm ITRS node) are shown to be consistent with experimental data for present-day long-channel devices, supporting our approach and conclusions.**

***Index Terms*—Contact resistance, field-effect transistor (FET), graphene, gate resistance, high-frequency behavior, MoS_2, radio-frequency (RF) behavior, two-dimensional transistors, unity-current-gain frequency, unity-power-gain frequency.**

I. Introduction

THE high-speed electronic properties of graphene, including a linear band dispersion with high band-structure velocity [1], record mobility [2], and record current density [3], have all contributed to the intense interest toward its use as a channel material for field-effect transistors (FETs) [4], [5]. At the same time, graphene has no electronic bandgap, which leads to the undesirable outcome that graphene FETs (GFETs) cannot be turned off, and hence that digital circuits cannot be created from graphene, except through modified forms having induced bandgaps, such as ribbons [6], bilayers [7], and antidot lattices [8].

In order to exploit the high-speed properties of graphene, the focus of research on single-layer GFETs[1] has thus leaned toward their use in analog radio-frequency[2] (RF) applications [9]. The measured values of the unity-current-gain (cutoff) frequency (f_T) have reached over 400 GHz [10], comparable to the fastest high-electron-mobility transistors (HEMTs) with similar gate lengths [11]. The observed values of the unity-power-gain frequency ($f_{\max}$) have been somewhat lower, due to the stronger influence of a lack of a bandgap, and hence low output conductance, on power gain vs. current gain [12], but they still hold promise, especially considering the relative immaturity of GFET technology, with a record value of around 70 GHz [13].

Although the mobility and high band-structure velocity of graphene have been repeatedly suggested [10], [14], [15] as being the main reason for its consideration for electronics, far more important is the ideal electrostatic environment inherent in two-dimensional materials [4]. Two-dimensional materials can be considered the ultimate form of the ultra-thin-body, silicon-on-insulator (UTB-SOI) transistor, a structure that allows for better electrostatic gate control than bulk materials, and hence more efficient downscaling while avoiding short-channel effects. Many two-dimensional materials have also been demonstrated to exhibit a high degree of mechanical strength and

Manuscript received July 15, 2016; accepted September 28, 2016. Date of publication November 18, 2016; date of current version January 6, 2017. This work was supported by the Natural Sciences and Engineering Research Council of Canada, by Alberta Innovates—Technology Futures, and by Alberta Innovation & Advanced Education. The review of this paper was arranged by Associate Editor L. Pierantoni.

K. D. Holland, M. Wong, S. Rizwan, and M. Vaidyanathan are with the Department of Electrical and Computer Engineering, University of Alberta, Edmonton, AB T6G 2V4, Canada (e-mail: maniv@ualberta.ca).

A. U. Alam was with the Department of Electrical and Computer Engineering, University of Alberta, Edmonton, AB T6G 2V4, Canada. He is now with Lumerical Solutions, Inc., Vancouver, BC V6E 3L2, Canada.

N. Paydavosi was with the Department of Electrical and Computer Engineering, University of Alberta, Edmonton, AB T6G 2V4, Canada. He is now with Intel Corporation, Hillsboro, OR 97124 USA.

C. M. Rogers was with the Department of Electrical and Computer Engineering, University of Alberta, Edmonton, AB T6G 2V4, Canada. He is now with the Edward L. Ginzton Laboratory, Stanford University, Stanford, CA 94305 USA.

D. Kienle is with Theoretische Physik I, Universität Bayreuth, Bayreuth 95440, Germany.

Digital Object Identifier 10.1109/TNANO.2016.2630698

[1] In this paper, we consider GFETs made only with graphene in its single-layer form; hence, "graphene" always means "single-layer graphene," even when not explicitly stated.

[2] In this paper, we use the terms "radio-frequency" and "high-frequency" interchangeably.

flexibility [16]–[18]. Such properties naturally lead to an interest not only in incorporating two-dimensional materials in traditional integrated circuit design, but also in the exciting area of flexible electronics [19].

Single-layer molybdenum disulphide (SL MoS_2) has been suggested as an alternative two-dimensional material to graphene, mostly because it exhibits a substantial bandgap of 1.8 eV [20], while still demonstrating the inherent electrostatic benefits of a two-dimensional material. On-off current ratios ($I_{\rm on}/I_{\rm off}$) of more than 10^7 have been demonstrated [21], much better than the values of 10^0–10^2 demonstrated for graphene [4]. An additional benefit of SL MoS_2 is that the existence of a bandgap may allow for improved RF performance in comparison to graphene transistors, through a reduction in the output conductance. However, to date, the experimentally observed values of f_T and $f_{\max}$ for SL MoS_2 transistors have been limited to 6.7 GHz and 5.3 GHz, respectively [22], while multi-layer MoS_2 (ML MoS_2) transistors have achieved f_T and $f_{\max}$ values of 42 GHz and 50 GHz [23], respectively. It has also been suggested that MoS_2 transistors will not be able to operate at high frequencies [24], and that graphene will hence remain the superior choice from this perspective.

A major limitation on the performance of single-layer materials for radio-frequency (RF) applications arises from the high values of contact resistance ρ_C determining the source and drain parasitic resistances. In graphene, for which preliminary work has been done to examine the impact of the contact resistance on RF metrics [12], [25], [26], the minimum achieved contact resistance has been around 100 $\Omega \cdot \mu$m, as evidenced by multiple experiments [27]–[29]. In SL MoS_2, creating high-quality, low-resistance ohmic contacts is a greater problem, due to the large bandgap combined with Fermi-level pinning [30]. Scandium [30], molybdenum [31], and graphene [32] have all been suggested as possibilities for the contact material. However, for each possibility, the contact resistance is above 1 k$\Omega \cdot \mu$m [33], an order of magnitude worse than what has been observed in graphene. Significantly lower (improved) contact resistances have been realized in ML MoS_2; chloride-doped devices have reached values below 500 $\Omega \cdot \mu$m [34], devices with nickel-etched graphene electrodes have reached values of 200 $\Omega \cdot \mu$m [27], and devices using the metallic phase of MoS_2 for contacts have reached values of less than 100 $\Omega \cdot \mu$m [21].

Given the attractive properties of SL MoS_2 for digital applications, an open question is whether or not its analog RF performance could match or even exceed that of graphene. If so, the idea of using SL MoS_2 in mixed-signal flexible electronics would become extremely attractive.

Work has already been done in comparing noise in the two materials. Currently, graphene has better $1/f$ [35] noise compared to SL MoS_2 [36], though an improvement in the $1/f$ noise in SL MoS_2 is expected with encapsulation of the channel and optimizations in processing to reduce trap density. The larger contact resistance in SL MoS_2 also degrades its $1/f$ noise [36], [37].

While noise is an important consideration, in this work, we focus on comparing the RF performance of SL MoS_2 with that of graphene by examining the achievable f_T and $f_{\max}$, addressing the fundamental question of whether the f_T and $f_{\max}$ of SL MoS_2 could meet or even exceed that of graphene, and if so, under exactly what conditions. We begin with a summary of the performance parameters that are determined by transport through the core of the transistor; these are the transconductance g_m, internal gate capacitance $C_{\rm gg}$, and output conductance g_o. We use this as a basis to examine the overall RF performance, including parasitics, via a comparison of the f_T and $f_{\max}$. First, we demonstrate that SL MoS_2 lags graphene in terms of *peak* performance, *i.e.*, the best performance attainable over all bias conditions, as measured by the peak values of f_T and $f_{\max}$. We show that this lag stems largely from the poorer values of ρ_C presently attainable with SL MoS_2, and we specify the values of ρ_C that SL MoS_2 would need to achieve to match graphene's peak capabilities. Second, we point out that under conditions of constrained bias current, SL MoS_2 looks far more competitive. We use the technologically relevant value of 1.65 mA/μm [38] and show that graphene loses much of its advantage due to a reduction of its g_m once the current is constrained. With the bias current constrained, we show that SL MoS_2 can meet or exceed graphene's performance by achieving contact resistances already attained in ML MoS_2. Overall, our work hence specifies exactly how the f_T and $f_{\max}$ of graphene and SL MoS_2 compare, with detailed discussion to support the conclusions.

This paper is organized as follows. Section II briefly describes our approach, which is based on a quantum-mechanical simulation of a common device structure differing only in the channel material; a quantum-mechanical simulation is essential for small gate lengths as well as for gapless materials. Section II also discusses the inclusion of all the parasitic resistances and capacitances, which are required for a realistic assessment. Section III examines the RF parameters determined by transport through the critical part of the common device structure; we consider the g_m, $C_{\rm gg}$, and g_o. Sections IV and V consider the *peak* (over all bias conditions) values of f_T and $f_{\max}$, with an emphasis on the impact of ρ_C, and Section VI reexamines the situation under the constraint of a fixed bias current. Finally, Section VII shows the validity of our approach through a comparison of our simulation results with experimental data available in the literature. The conclusions of our study are summarized in Section VIII.

II. Approach

A. Comparison Methodology

In order to make a fair and direct comparison of the RF performance between SL MoS_2 and graphene transistors, we simulate the same device structure for both materials, including the dimensions of the metal contacts, the thickness of the gate-oxide layer, and the type and thickness of the substrate; the only difference is the channel material itself. The common structure is shown schematically in Fig. 1. Key physical parameters are summarized in Tables I and II, and they are derived from the ITRS 7-nm node [38]. We assume the channel region is surrounded by degenerately n-doped source and drain reservoirs with an abrupt or step-like doping profile, and that the device is "MOSFET-like," where the source and drain contacts are ohmic and the gate modulates the source-to-channel barrier. These simplifications allow us to comparatively assess

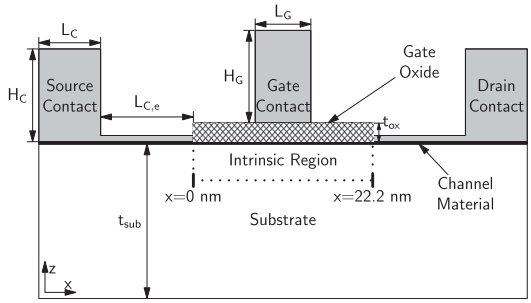

Fig. 1. Common device structure used in this study. The dimensions are given in Tables I and II. The dotted lines show a cross-section of the intrinsic portion of the device, defined as the core of the structure excluding parasitics. This core contains the 10.2-nm intrinsic channel along with 6-nm-long portions of the degenerately n-doped source and drain reservoirs. The source and drain contact geometries are symmetric with respect to the gate. The positions $x = 0$ and $x = 22.2$ nm, which delimit the intrinsic region, are labeled for later reference.

TABLE I
STRUCTURE PARAMETERS

Parameter	Description	Value
L_G	Physical Gate Length	12.7 nm
$L_{\rm ch}$	Effective Channel Length	10.2 nm
$V_{\rm DD}$	Power Supply Voltage	0.78 V
$K_{\rm ox}$	Gate Dielectric Constant	15.0
$t_{\rm ox}$	Physical Oxide Thickness	2.46 nm
$t_{\rm sub}$	Substrate Thickness	50 nm
$K_{\rm sub}$	Substrate Dielectric Constant	3.9

TABLE II
EXTERNAL STRUCTURE PARAMETERS

Parameter	Description	Range [nm]
H_G	Gate Height	10–50
H_C	S/D Contact Height	10–50
L_C	S/D Contact Length	100–1000
$L_{\rm C,e}$	S/D Extension Length	10–30

the best-case performance of each channel material, consistent with the aim of this study. In this regard, it is worth mentioning that while it is common in experiments to utilize electrostatic doping with a back gate, promising techniques exist to dope graphene and MoS_2 [39], [40], and that while it is more common to realize Schottky-barrier transistors in experiments, progress toward "MOSFET-like" devices with ohmic contacts have been demonstrated for both graphene and ML MoS_2 [41], [42].

B. Analysis of Transport

1) Overview: The transport is modeled with a quantum-mechanical device simulator that solves the Poisson equation (along x and z) self-consistently with the non-equilibrium Green's function (NEGF) formalism [43] (along x). The tool simulates electron transport within the dotted region of Fig. 1, the critical active region of the transistor, which we call the "intrinsic region," to extract the bias-dependent circuit elements for use in the dashed portion of the small-signal equivalent circuit of Fig. 2. For the purposes of this study, the simulations were carried out under ballistic conditions for graphene and *with* phonon scattering for SL MoS_2. This approach is justified

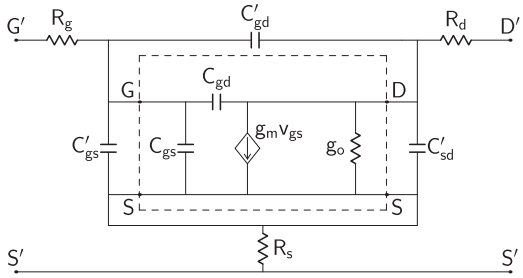

Fig. 2. Equivalent circuit used in this study, with the intrinsic portion boxed. The labels S, D, and G refer to the source, drain, and gate terminals, respectively, of the intrinsic device, while their primed counterparts S', D', and G' refer to the corresponding extrinsic device terminals.

by the effective channel length of 10.2 nm in our structures. Graphene has been shown to exhibit ballistic transport on the micrometer scale [44], while the mean-free path for SL MoS_2 is over 14 nm [45] for low-field conditions, but can be as low as 7.5 nm under higher electric fields [46]. Both elastic (transverse and longitudinal acoustic) and inelastic (longitudinal optical, homopolar, and Fröhlich interaction) scattering are modeled in SL MoS_2 [45], [47].

2) Poisson Solver: The Poisson equation, discretized with finite differences, is used in the electrostatic simulation of both devices. We assume that the device is wide and that the potential along the width of the channel (along y) does not vary, meaning that the simulation does not account for the effects of the edges. A two-dimensional computational domain, in the x-z plane, is hence used to capture electrostatic effects in the relevant regions, similar to the standard analysis of CMOS devices.

3) NEGF Solver: For SL MoS_2 devices, the NEGF solver utilizes a discretized effective-mass Hamiltonian with an effective mass of $m^* = 0.55m_e$ [48], where $m_e = 9.11 \times 10^{-31}$ kg is the free-electron rest mass. We verified that under all bias conditions, and for energies relevant to transport, the conduction band follows a parabolic dispersion, hence justifying this approach. The NEGF equations are solved in one dimension (along x), with the contribution of transverse modes (along y) being taken into account by using the Fermi-Dirac integral of order $-1/2$, as in [49]. The contact self-energies are computed analytically because of the simple form of the one-dimensional Hamiltonian [43].

A nearest-neighbor, tight-binding Hamiltonian with a p_z-orbital basis is used in the graphene simulation [50], an approach that natively captures the effect of Klein tunneling. Bloch boundary conditions are imposed in the transverse direction (along y), giving a series of orthogonal one-dimensional transport modes (along x). The contact self-energies are computed numerically with the Sancho-Rubio iterative method [51].

In both materials, the NEGF equations are solved using the recursive Green's function technique [52].

C. Inclusion of Parasitics

1) Our Approach: We used parasitic capacitances and resistances, extracted or calculated as described further below, in conjunction with the values of the transport-dependent parameters g_m, g_o, and $C_{\rm gg}$, to find the RF figures of merit f_T and

$f_{\max}$ for the overall transistor by simulation of the transistor equivalent circuit (Fig. 2).

In order to quantify the effects of contact resistance, we extract the extrinsic figures of merit f_T and $f_{\max}$ from the transistor equivalent circuit as a function of realized contact resistance ρ_C: $f_T(\rho_C)$ and $f_{\max}(\rho_C)$. This is accomplished by assuming the device width (into the page) in Fig. 1 is $W = 1\,\mu$m, as we have already mentioned, and hence setting $R_s = R_d = R_C$, with $R_C = \rho_C/1\,\mu$m, in the circuit. It is important to note that the use of $W = 1\ \mu$m to extract $f_T(\rho_C)$ and $f_{\max}(\rho_C)$ incurs no loss of generality, since all the parameters in the circuit, from which the figures of merit are obtained, scale with W in such a way so as to leave $f_T(\rho_C)$ and $f_{\max}(\rho_C)$ unaffected by the value of W. We explicitly verified this to be the case, but it can also be seen, for example, by inspection of (1) and (2) further below; all terms in the numerator and denominator can be shown to scale proportionally or inversely with W, such that the final result is unaffected. Hence, in what follows, we consider $f_T(\rho_C)$ and $f_{\max}(\rho_C)$ as general measures of the RF performance that could be achieved for realized values of ρ_C, with all parasitic capacitances and resistances corresponding to $W = 1\,\mu$m, and we focus on how graphene and SL MoS_2 compare as a function of ρ_C.

2) Capacitances: The parasitic capacitances $C'_{\rm gd}$, $C'_{\rm gs}$, and $C'_{\rm sd}$ in the circuit of Fig. 2 are found by simulating an open structure; the open structure includes the entire device in Fig. 1, with the exclusion of the channel material. The capacitances are measured using COMSOL Multiphysics [53] by applying a small voltage to one contact and measuring the induced charge on the other contacts, one at a time. Since we are using identical structures for each channel material, the values for the parasitic capacitances with SL MoS_2 and graphene will be the same. In addition to the assumed device width of 1 μm, a few other parameters needed for the extraction are specified by the ITRS [38] for the 7-nm node, as provided in Table I. Beyond these specified parameters, those remaining are the length and height of the source and drain contacts (L_C and H_C), the height of the gate contact (H_G), and the length of the metal extension regions ($L_{\rm C,e}$). Unfortunately, the exact values of these dimensions for the 7-nm node are uncertain. Due to this uncertainty, we have simulated different combinations of H_C, H_G, $L_{\rm C,e}$, and L_C; the range of simulated values can be found in Table II. We found that these figures of merit deviated by no more than five percent about their average values as a function of the capacitances, holding the other parameters fixed and as the capacitances varied over the range of dimensions specified in Table II.[3] Given the small deviation of $\pm 5\%$, there is hence no loss of generality in using the average values over capacitance as representative of the RF performance, and these are therefore the values presented in the following sections.

3) Contact Resistance: The parasitic resistances R_s, R_d, and R_g of the source, drain, and gate, respectively, are included in the circuit of Fig. 2. The considerable impact of these resistances on high-frequency operation motivates us to treat them as key parameters in our study. Appropriate values can be computed by knowing contact resistance and the device geometry.

The values of realized contact resistance ρ_C are typically quoted in the literature in the units of $\Omega \cdot \mu$m; the corresponding resistance values R_s and R_d determining RF performance would be ρ_C divided by the device width (into the page) of $W = 1\,\mu$m in Fig. 1. This method of calculating R_s and R_d is justified since current crowding is consistently observed in single-layer devices; the current transfers over a characteristic length L_T [54]–[56], and contacts longer than L_T exhibit similar contact resistances that depend only on width [57]. L_T is estimated to be 200–520 nm for graphene [54] and 74–630 nm for SL MoS_2 [58], [59]. The results in this paper hence strictly apply to structures having $L_C \geq L_T$, although this is not a limitation, since $L_C \geq L_T$ would be required to keep the contact resistance low to optimize RF performance.

4) Gate Resistance R_g: The gate resistance is strongly dependent on the physical layout of the device, and it can be minimized by the use of multiple gate fingers in parallel. In this way, the value of gate resistance can be reduced to the order of a few ohms. Due to the flexibility in achieving desired gate resistance via appropriate layout, we treat the gate resistance as a parameter, with values ranging from 0.1 Ω to 1 kΩ. We will return to this point in Section V-B.

III. Summary of Transport-Dependent RF Performance

The first step in comparing the overall potential of the two materials is to investigate the RF parameters arising from transport within the critical (intrinsic) operating region of the common device structure, *i.e.*, within the dotted portion of Fig. 1. These parameters are the transconductance g_m, the internal gate capacitance $C_{\rm gg} = C_{\rm gs} + C_{\rm gd}$, and the output conductance g_o, and the corresponding circuit elements are those within the dashed portion of Fig. 2. We will keep the discussion in this section very brief; those familiar with the results can skip to Section IV.

A. Terminal Characteristics

For reference, we begin with the simulated terminal characteristics of the intrinsic device for the two channel materials, as shown in Fig. 3(a). A few features are immediately visible. First, for biasing determined by the same voltages, *e.g.*, $(V_{\rm GS}, V_{\rm DS}) = (V_{\rm DD}/2, V_{\rm DD}/2)$, where $V_{\rm DD} = 0.78$ V [38], as circled on the curves, graphene yields much higher current densities. Second, the lack of a bandgap in graphene causes the characteristics never to fully saturate, whereas the curves for SL MoS_2 do saturate, a fact that is well known, but which we point out for completeness. The inset to the figure illustrates the reduction in current with phonon scattering vs. ideal ballistic transport in SL MoS_2.

B. Transconductance and Gate Capacitance

Fig. 3(b) shows g_m and $C_{\rm gg}$ for both materials as a function of $V_{\rm GS}$, with $V_{\rm DS}$ held at $V_{\rm DD}/2$. The g_m is significantly higher in graphene, with the small equivalent oxide thickness (EOT) of 0.64 nm specified for the 7-nm node mitigating any reduction in transconductance that could arise due to short-channel effects

[3]The capacitances themselves varied as follows: $C'_{\rm sd}$ varied from 35 to 65 aF/μm, and $C'_{\rm gs}$ and $C'_{\rm gd}$ varied from 99 to 124 aF/μm.

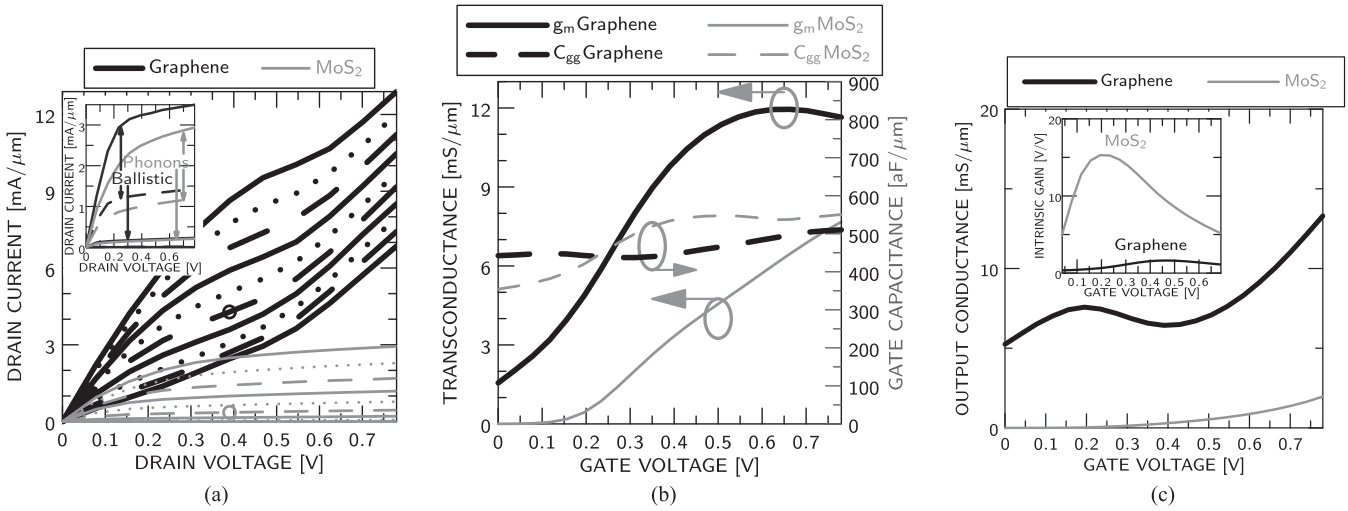

Fig. 3. Summary of transport-dependent RF performance metrics. (a) Current-voltage relationships for graphene and SL MoS_2 found from a transport simulation of the dotted portion of Fig. 1, shown for gate voltages ranging from $V_{\rm GS} = 0.078$ to $V_{\rm GS} = V_{\rm DD} \equiv 0.78$ V [38] in increments of 0.078 V. The circles on each set of curves indicate the locations of a representative bias point corresponding to applied voltages $V_{\rm GS} = V_{\rm DS} = V_{\rm DD}/2$. The inset to the figure shows the current including phonon scattering vs. ballistic transport for SL MoS_2. (b) Transconductance g_m and gate capacitance $C_{\rm gg}$ vs. gate voltage $V_{\rm GS}$ for graphene and SL MoS_2. The drain voltage is held at $V_{\rm DS} = V_{\rm DD}/2$, where $V_{\rm DD} = 0.78$ V [38]. (c) Output conductance g_o vs. gate voltage $V_{\rm GS}$ for graphene and SL MoS_2. The drain voltage is held at $V_{\rm DS} = V_{\rm DD}/2$, where $V_{\rm DD} = 0.78$ V [38]. The inset to the figure is the available voltage gain $A_v = g_m/g_o$ vs. $V_{\rm GS}$ for both materials, under the same value of $V_{\rm DS}$.

caused by Klein tunnneling [38], [60]. On the other hand, $C_{\rm gg}$ is similar in magnitude for the two materials. The similarity in $C_{\rm gg}$ is a direct outcome of employing identical gate structures for both channel materials in Fig. 1, leading to identical gate-oxide capacitance values. For both materials, the gate-oxide capacitance dominates $C_{\rm gg}$, with the quantum capacitance having only a secondary impact.

C. Output Conductance

It is well-known that the lack of a bandgap in graphene leads to poor output conductance [12]. The results in Fig. 3(c) confirm the expectation, showing that g_o in graphene is substantially worse than in SL MoS_2. The inset to the figure shows one immediate impact, which is to severely limit the available voltage gain $A_v = g_m/g_o$ in graphene, despite its higher g_m. The poor g_o of graphene has even further ramifications in determining its overall RF performance vs. SL MoS_2, once the impacts of parasitics are considered, as we will discuss in Section IV.

IV. Peak Unity-Current-Gain Frequency f_T

A. Definition

The f_T is found by extrapolating the magnitude of the common-source, small-signal current gain to unity. While we found f_T exactly, by simulation of the circuit in Fig. 2, a useful approximation is [61]

$$f_T \approx \frac{1}{2\pi} \frac{g_m}{C_{\rm gg,tot} + [g_o C_{\rm gg,tot} + g_m C_{\rm gd,tot}](R_s + R_d)} \quad (1)$$

where $C_{\rm gg,tot} \equiv C_{\rm gg} + C'_{\rm gs} + C'_{\rm gd}$ is the total gate capacitance and $C_{\rm gd,tot} \equiv C_{\rm gd} + C'_{\rm gd}$ is the total gate-drain capacitance. This expression serves to illustrate how the transport-dependent circuit elements g_m, g_o, and $C_{\rm gg}$ discussed in Section III *interact* with the parasitics to degrade the high-frequency performance of the transistor, and we will refer to it as needed in the remainder of this paper.

In this section, we will focus on the *peak* value of f_T, where "peak" means "absolute maximum" over all gate and drain bias voltages, $0 \le V_{\rm GS} \le V_{\rm DD}$ and $0 \le V_{\rm DS} \le V_{\rm DD}$, with $V_{\rm GS}$ and $V_{\rm DS}$ referring to the biases used across the internal transistor (within the dotted portion of Fig. 1) to determine the internal transistor components (within the dashed lines of Fig. 2). Later, in Section VI, we will consider the value of f_T under the condition of a fixed bias current.

B. General Behavior vs. ρ_C

Fig. 4 shows a plot of the peak $f_T(\rho_C)$ vs. the contact resistance ρ_C determining R_s and R_d in the two materials. We have indicated several important pieces of information on the plot.

1) Solid curves are used to show the peak $f_T(\rho_C)$ with no simplifications.
2) Dotted curves are used to show the value of the peak $f_T(\rho_C)$ when neglecting the effect of the output conductance g_o, in order to assess the role of the bandgap in each material.
3) Short-dashed vertical lines are used to indicate the best contact resistances realized to date in graphene and SL MoS_2 of 100 $\Omega \cdot \mu$m [27] and 1 k$\Omega \cdot \mu$m [33], respectively.
4) A long-dashed vertical line is used to indicate 30 $\Omega \cdot \mu$m, the theoretical minimum contact resistance in graphene [28]. We add that 30 $\Omega \cdot \mu$m represents a lower bound on the contact resistance for both materials, as it is unlikely that contacts to SL MoS_2 could ever achieve the same efficiency as contacts to graphene.
5) Horizontal lines are used to indicate the peak intrinsic (neglecting all parasitics) cutoff frequency, given by $f_{\rm T,int} = g_m/2\pi C_{\rm gg}$, for each material.

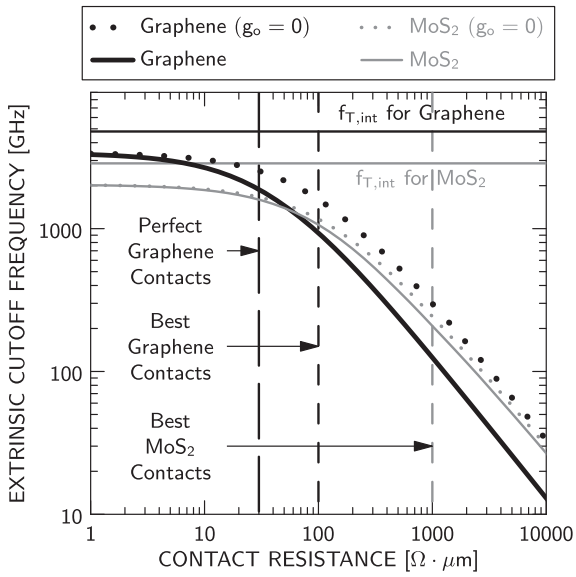

Fig. 4. Plot of the peak (absolute maximum) unity-current-gain frequency $f_T(\rho_C)$ for SL MoS_2 and graphene vs. the contact resistance ρ_C determining the drain and source resistances R_s and R_d (solid curves). The values of peak $f_T(\rho_C)$ are found assuming a device width of 1 μm, as discussed in the text of Section II-C. The dotted curves show the values when neglecting the effect of the output conductance g_o. The best contact resistances achieved to date in the two materials are represented by the short-dashed vertical lines, and the resistance for perfect graphene contacts are indicated by a long-dashed vertical line. The peak intrinsic cutoff frequency $f_{\text{T,int}} = g_m/2\pi C_{\text{gg}}$, *i.e.*, the peak cutoff frequency neglecting all parasitics, is indicated for each device with a horizontal line at the top of the figure.

Since Fig. 4 embeds several pieces of information, it will be most convenient to discuss the various aspects one at a time, and then to gather together the most important outcomes.

C. Performance Ceiling

The values of the peak intrinsic cutoff frequency $f_{\text{T,int}} = g_m/2\pi C_{\text{gg}}$ indicated by the horizontal lines in Fig. 4 can be considered as measures of the "raw speed" of each material, as determined by *transport effects* in the transistor channel, and excluding the detrimental effects of the output conductance g_o and parasitics. From Fig. 3(b), since the internal gate capacitance C_{gg} is similar for both materials, the raw speeds are determined primarily by the peak values of g_m. The higher peak g_m in graphene gives it a higher performance ceiling.

D. Behavior for Low and High Contact Resistance

A severe reduction in the peak $f_T(\rho_C)$ with increasing contact resistance ρ_C is observed in Fig. 4 for both materials, as shown by the monotonically decreasing (moving to the right) solid curves, highlighting the need to keep ρ_C as low as possible. It is worth noting that achieving zero contact resistance does not mean the $f_T(\rho_C)$ will equal the performance ceiling indicated by the intrinsic limit $f_{\text{T,int}}$; the presence of parasitic capacitances will by themselves cause the peak $f_T(\rho_C)$ to fall short of the intrinsic limit $f_{\text{T,int}}$, even when $\rho_C \to 0$, as illustrated by the behavior of the solid curves on the far left side of Fig. 4. We found that the parasitic capacitances C'_{gs}, C'_{gd}, and C'_{sd} cause a uniform degradation of the curves in Fig. 4 for both graphene and SL MoS_2 (from where they would otherwise be) by about 30%.

E. Effect of g_o

For graphene, a substantial reduction in peak $f_T(\rho_C)$ is observed when accounting for the effect of g_o, as evidenced by the large gap between the solid and dotted graphene curves in Fig. 4. For example, at today's best contact resistance of $\rho_C = 100\,\Omega \cdot \mu$m, the reduction in peak $f_T(\rho_C)$ in graphene due to g_o is around 700 GHz, from 1.6 THz to 900 MHz, representing a degradation of 40%. This g_o-driven reduction is more severe than we have previously calculated for longer channel devices [12], suggesting that single-layer GFETs may not scale well to lower technology nodes. The reduction can be viewed as arising from the $g_o(R_s + R_d)$ term in the denominator of (1), where $R_s = R_d = \rho_C/1\,\mu$m; only when $\rho_C \to 0$ can the reduction be neglected, as shown by the merging of the solid and dotted graphene curves for low ρ_C in Fig. 4.

For SL MoS_2, the impact of g_o on peak $f_T(\rho_C)$ is negligible, as evidenced by the strong overlap between the solid and dotted SL MoS_2 curves in Fig. 4. As might be expected, the large bandgap in SL MoS_2 keeps g_o sufficiently low to have a negligible impact, even in the presence of phonon scattering, which we have included for SL MoS_2.

F. Comparison with Identical Contact Resistance

The peak $f_T(\rho_C)$ of SL MoS_2 is higher than in graphene for any fixed and identical contact resistance greater than $60\,\Omega \cdot \mu$m, as shown by the relative positions of the solid curves in Fig. 4 for $\rho_C > 60\ \Omega\ \cdot \mu$m. For contact resistances less than $60\ \Omega \cdot \mu$m, a *crossover* is observed, and graphene's peak $f_T(\rho_C)$ is higher. The crossover is due to different trends in the behavior of the peak $f_T(\rho_C)$ in the two materials. In graphene, a larger peak $f_T(\rho_C)$ is observed for low ρ_C due to a large g_m, followed by a *rapid decline* in the peak $f_T(\rho_C)$ with ρ_C due to a large g_o (interacting with R_s and R_d resulting from ρ_C). In SL MoS_2, a lower peak $f_T(\rho_C)$ due to a smaller g_m is observed for low ρ_C, followed by a *shallower decline* in peak $f_T(\rho_C)$ with ρ_C due to a small value of g_o. The crossover value of $60\ \Omega \cdot \mu$m is only slightly larger than the theoretical minimum contact resistance of graphene [28], meaning that for *fixed and realizable (above the theoretical minimum)* common values of ρ_C in the two materials, we can say that the peak $f_T(\rho_C)$ in SL MoS_2 will typically be higher than, and at least roughly equal to, that of graphene.

G. Comparison with Present-Day Contact Resistance

The greater performance potential for SL MoS_2 at common values of ρ_C, indicated by the relative positions of the solid curves in Fig. 4 for $\rho_C > 60\,\Omega \cdot \mu$m, is difficult to realize, because the processing steps are not yet available to make similar quality contacts for both materials in their single-layer forms. As discussed in Section I, contact resistance in single-layer graphene is currently a factor of ten lower than in SL MoS_2. Using the best achieved contact resistance to date for each single-layer material, Fig. 4 indicates a peak $f_T(\rho_C)$ of 930 GHz for

graphene at $\rho_C = 100\,\Omega \cdot \mu$m and 210 GHz for SL MoS_2 at $\rho_C = 1\,\text{k}\Omega \cdot \mu$m.

In order for SL MoS_2 to achieve graphene's value of 930 GHz, the contact resistance would have to be lowered below $130\,\Omega \cdot \mu$m. Unfortunately, $130\,\Omega \cdot \mu$m is far better than the best achieved to date for SL MoS_2 transistors; fortunately, it is also *worse* than the best achieved value of $100\,\Omega \cdot \mu$m in ML MoS_2, suggesting ML MoS_2 as a potential path forward to get the peak performance of MoS_2 devices closer to what can presently be achieved with graphene.

H. Possibility of THz f_T

The possibility of achieving a peak unity-current-gain frequency of at least 1 THz is an important technological barrier. Even with the large reduction in peak $f_T(\rho_C)$ due to the poor output conductance in graphene, a value of 1 THz is achievable if ρ_C could be made below $90\,\Omega \cdot \mu$m, which represents an incremental improvement over current graphene contact resistances. On the other hand, for SL MoS_2, the contact resistance would need to be made below $100\,\Omega \cdot \mu$m, a considerably more daunting task, but possible for ML MoS_2.

I. Outcomes

Based on the detailed points above, Fig. 4 points to the following important outcomes.

1) For any *common* value of contact resistance greater than $\rho_C = 60\,\Omega \cdot \mu$m, SL MoS_2 would exhibit a higher peak unity-current-gain frequency, with graphene suffering from the deleterious effects of its poor output conductance.
2) However, at present, SL MoS_2 suffers from much poorer contact resistances. As a result, the peak performance of graphene remains superior if one compares the performance using the *best* ρ_C values achieved to date. The contact resistance of SL MoS_2 would have to be lowered considerably to match graphene.
3) For devices corresponding to the 7-nm technology node [38], peak values of f_T of 1 THz or above can be achieved in both materials, but this barrier is more easily reached with graphene, requiring only an incremental improvement in contact resistance from what has been achieved to date.

V. Peak Unity-Power-Gain Frequency $f_{\max}$

A. Definition

The $f_{\max}$ is calculated by extrapolating Mason's unilateral gain (U) [62] to unity. While we found $f_{\max}$ exactly through simulation of the circuit in Fig. 2, a useful approximation is [61]

$$f_{\max} \approx \frac{f_T}{\sqrt{[4g_o + 8\pi f_T C_{\text{gd,tot}}]\,R_g + [\alpha_M 8\pi f_T C_{\text{gd,tot}}]\,R_d}} \tag{2}$$

where

$$\alpha_M \equiv \frac{C_{\text{gd,tot}} + C'_{\text{sd}}}{C_{\text{gg,tot}}}. \tag{3}$$

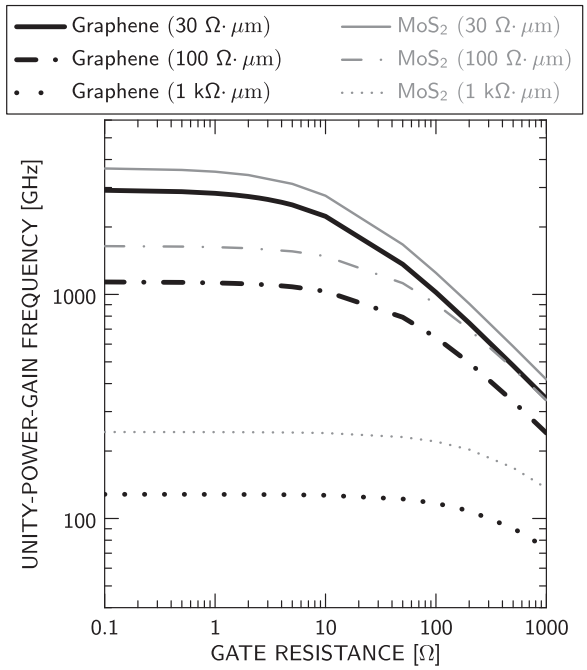

Fig. 5. Peak (absolute maximum over all bias voltages) unity-power-gain frequency $f_{\max}(R_g)$ vs. gate resistance R_g for graphene and MoS_2. Separate curves are shown for values of contact resistance ρ_C equal to $30\,\Omega \cdot \mu$m, $100\,\Omega \cdot \mu$m, and $1\,\text{k}\Omega \cdot \mu$m.

A lone factor of f_T is found in the numerator of (2), meaning that the two terms in the denominator, one depending on R_g and the other on $R_d = \rho_C/1\,\mu$m, can be conceptualized as *modifying* the f_T to arrive at a value of $f_{\max}$. We will refer to this expression as needed in the remainder of this paper.

In this section, we will consider the peak $f_{\max}$, where "peak" means "absolute maximum" over all gate and drain bias voltages, $0 \le V_{\text{GS}} \le V_{\text{DD}}$ and $0 \le V_{\text{DS}} \le V_{\text{DD}}$. Later, in Section VI, we will consider the $f_{\max}$ under the constraint of a fixed bias current.

B. Effect of Gate Resistance

In contrast to the negligible impact the gate resistance R_g has on f_T, it is an important quantity when considering $f_{\max}$. Fig. 5 shows a plot of peak $f_{\max}$ vs. gate resistance R_g, which we denote as $f_{\max}(R_g)$ vs. R_g. Results are shown for various assumed values of contact resistance ρ_C, where ρ_C determines R_s and R_d. Three sets of curves are marked, representing the best contact resistances realized to date in SL MoS_2 ($1\,\text{k}\Omega \cdot \mu$m) and graphene ($100\,\Omega \cdot \mu$m) and the theoretical minimum contact resistance achievable in graphene ($30\,\Omega \cdot \mu$m).

It is well-known that the gate resistance can be reduced by appropriate layout techniques. Fig. 5 shows that as R_g is reduced, $f_{\max}(R_g)$ *saturates* to a maximum value, with the value of R_g needed for the saturation determined by the value of ρ_C. Higher values of ρ_C cause the saturation to occur at higher values of R_g. Such behavior is expected from (2), as reducing R_g in the denominator becomes less important when the term involving $R_d = \rho_C/1\,\mu$m is larger.

Note that for every value of ρ_C used in Fig. 5, the corresponding curve can be taken to be saturated for values of $R_g = 1\,\Omega$ or

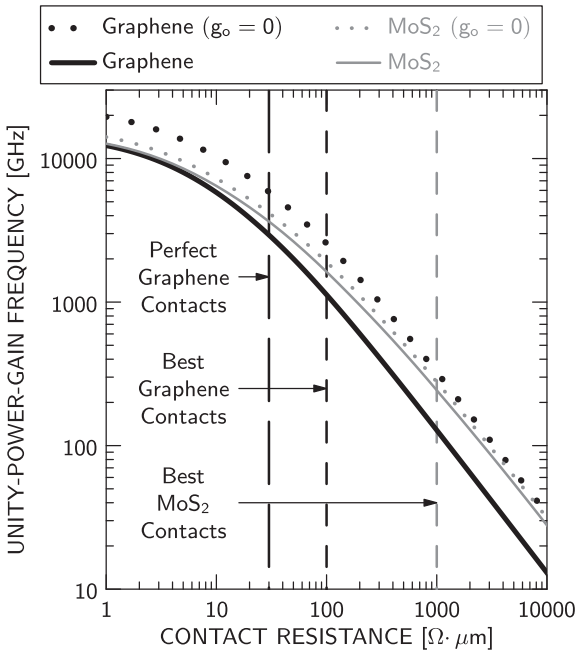

Fig. 6. Peak unity-power-gain frequency $f_{\max}(\rho_C)$ vs. the contact resistance ρ_C determining the source and drain resistances R_s and R_d, with R_g held at $1\,\Omega$, as discussed in the text.

lower. Given that values of gate resistance as low as $R_g = 3\,\Omega$ have already been achieved for 7-μm-wide graphene devices with two gate fingers [13], and since we are interested in best performance, it is hence convenient for the remainder of this discussion to use $R_g = 1\,\Omega$.

C. General Behavior vs. ρ_C

Fig. 6 shows a plot of the peak $f_{\max}(\rho_C)$ vs. contact resistance ρ_C, found with a gate resistance $R_g = 1\,\Omega$, and where $R_s = R_d = \rho_C/1\,\mu$m. As with Fig. 4 discussed earlier, we have included dotted curves to show the values of peak $f_{\max}(\rho_C)$ when neglecting the output conductance g_o, short-dashed vertical lines to indicate the best contact resistances realized to date, and a long-dashed vertical line to indicate the theoretical minimum contact resistance achievable in graphene.

As with the peak $f_T(\rho_C)$ in Fig. 4, Fig. 6 shows a severe reduction of the peak $f_{\max}(\rho_C)$ with increasing contact resistance ρ_C, again highlighting the need to keep ρ_C as low as possible.

Fig. 6 points to a number of other important features regarding the peak $f_{\max}(\rho_C)$, which we examine individually before summarizing the main outcome.

D. Effect of g_o

For graphene, the output conductance significantly reduces the peak $f_{\max}(\rho_C)$, as seen by comparing the solid and dotted graphene curves in Fig. 6; for example, at $\rho_C = 100\,\Omega \cdot \mu$m, it drops from 2.6 THz to 1.1 THz. Fig. 6 also shows that the effect of g_o on $f_{\max}(\rho_C)$ for graphene cannot be eliminated by minimizing the contact resistance, contrasting what we observed in Fig. 4 for the peak $f_T(\rho_C)$; specifically, the graphene curves in Fig. 6 with and without g_o do not converge at low values of contact resistance. This behavior can be attributed to the $g_o R_g$ product in the denominator of (2), which does not vanish even when $\rho_C \to 0$.

For SL MoS_2, the curves in Fig. 6 show that the reduction in peak $f_{\max}(\rho_C)$ due to g_o is small; a reduction of around 10% is observed for the range of contact resistances considered. As expected, the bandgap in SL MoS_2 keeps g_o sufficiently small for it to have a minimum impact, even in the presence of phonon scattering, which we have included for SL MoS_2.

E. Comparison with Identical Contact Resistance

For all identical values of ρ_C, the $f_{\max}(\rho_C)$ in SL MoS_2 is higher than in graphene, as shown by the solid curves in Fig. 6. It is also worth noting that unlike what we observed with the $f_T(\rho_C)$ in Fig. 4, there is no *crossover* of the graphene and SL MoS_2 performance curves at sufficiently low values of ρ_C. The lack of a crossover can be attributed to the $g_o R_g$ product in the denominator of (2), which persists in degrading the peak $f_{\max}(\rho_C)$ of graphene even when $\rho_C \to 0$, due to a pronounced g_o.

F. Comparison with Present-Day Contact Resistance

Current technology limits ρ_C to $100\,\Omega \cdot \mu$m in graphene and $1\ \text{k}\Omega \cdot \mu$m in SL MoS_2. With these different values of contact resistance, we find the peak $f_{\max}(\rho_C)$ values to be 1.1 THz for graphene (at $\rho_C = 100\,\Omega \cdot \mu$m) and 240 GHz for SL MoS_2 (at $\rho_C = 1\ \text{k}\Omega \cdot \mu$m).

Based on *current* contact technology, SL MoS_2 hence cannot match graphene. To reach graphene's value of 1.1 THz, MoS_2 would require a contact resistance below $160\,\Omega \cdot \mu$m, which has only been achieved with ML MoS_2.

G. Possibility of THz $f_{\max}$

Finally, both graphene and SL MoS_2 should be able to achieve a peak unity-power-gain frequency of 1 THz.

Graphene can achieve $f_{\max}(\rho_C) = 1$ THz operation with a contact resistance around $110\,\Omega \cdot \mu$m, which has already been achieved. However, reductions in the gate length and optimization in the gate layout will be needed; the current record of 70 GHz [13] was obtained with a gate length of 100 nm, an order of magnitude larger than the ITRS specifications for the 7-nm node [38] used as guidance for the work in this paper.

An $f_{\max}$ of 1 THz can be achieved in SL MoS_2 with contact resistances of approximately $170\,\Omega \cdot \mu$m, a value that has been achieved in multi-layer devices.

H. Outcome

The outcome from Fig. 6 regarding the peak $f_{\max}(\rho_C)$ largely mirrors what we saw in Section IV for the peak $f_T(\rho_C)$. Supported by the detailed discussion in this section, we can say that at identical contact resistances, SL MoS_2 would outperform graphene in terms of the peak $f_{\max}(\rho_C)$, but that MoS_2 contact technology simply lags that of graphene, such that with today's values of ρ_C, graphene retains the performance edge. Similarly, while THz operation should be possible in both

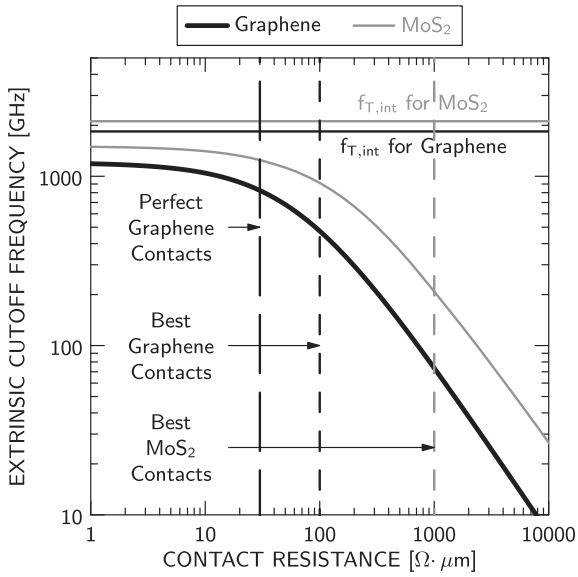

Fig. 7. Plot of the unity-current-gain frequency $f_T(\rho_C)$ for SL MoS_2 and graphene vs. the contact resistance ρ_C determining the source and drain resistances R_s and R_d (solid curves), found under the constraint of a bias current of 1.65 mA/μm. The values of $f_T(\rho_C)$ are found assuming a device width of 1 μm, as discussed in the text of Section II-C. The best contact resistances achieved to date for the two materials are represented by the short-dashed vertical lines, and the resistance for perfect graphene contacts are indicated by a long-dashed vertical line. The peak intrinsic cutoff frequency $f_{\text{T,int}} = g_m/2\pi C_{\text{gg}}$, *i.e.*, the peak cutoff frequency neglecting all parasitics, is indicated for each device with a horizontal line at the top of the figure.

materials, SL MoS_2 would require a substantial improvement in its contact resistance.

VI. Comparison With Equal Bias Currents

A. Motivation

Until this point, we have emphasized the comparison of *peak* performance (over all bias conditions) for graphene and SL MoS_2. However, the minimization of dc bias current is an important consideration (*e.g.*, to minimize the power drawn from the supply V_{DD}). For the 7-nm technology node, the minimum on current for a transistor is specified to be approximately 1.65 mA/μm [38]. We will now compare the f_T and $f_{\max}$ under the constraint that the devices each carry this bias current, although our results are independent of the exact value chosen.

We will consider the most important aspects of the f_T and $f_{\max}$ separately, and then state the main outcome.

B. Unity-Current-Gain Frequency $f_T(\rho_C)$

Fig. 7 shows a plot of the unity-current-gain frequency $f_T(\rho_C)$ vs. contact resistance ρ_C, *under the constraint of equal bias currents, set to 1.65 mA/μ m in both materials.* The following observations can be made and should be contrasted with the results from Fig. 4, which showed the *peak* $f_T(\rho_C)$ (over all bias conditions).

1) Performance Ceiling: Fig. 8 depicts the transconductance g_m vs. the bias current I_D. In contrast to Fig. 3(b) for equal *voltages*, under the constraint of equal bias currents, the g_m in MoS_2 will become larger than that in graphene. While the underlying physical details are outside the scope of the present paper, this reversal can be attributed to the presence of a bandgap and high density of states in SL MoS_2. The higher g_m in MoS_2 causes it to achieve a higher value of $f_{\text{T,int}} = g_m/2\pi C_{\text{gg}}$ than graphene. The higher $f_{\text{T,int}}$ is reflected in the horizontal lines in Fig. 7, which hence show a reversal in the trend we saw in Fig. 4 when considering peak performance over all bias conditions.

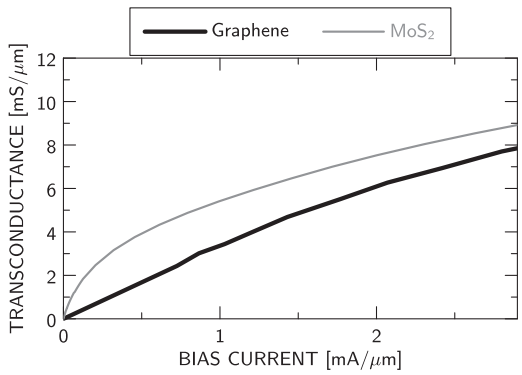

Fig. 8. Transconductance g_m vs. bias current I_D for graphene and SL MoS_2 transistors. The drain and gate voltages were adjusted to provide the largest possible value of g_m at each value of I_D.

2) Comparison with Present-Day Contact Resistance: With a bias current of 1.65 mA/μm, and for the best achieved contact resistance $\rho_C = 100\,\Omega\cdot\mu$m in graphene, the $f_T(\rho_C)$ in graphene drops nearly 50%, from its peak value of 930 GHz in Fig. 4 to a current-constrained value of 475 GHz in Fig. 7. On the other hand, for SL MoS_2, at the best-achieved contact resistance of $\rho_C = 1\,\text{k}\Omega\cdot\mu$m, the $f_T(\rho_C)$ in Figs. 4 and 7 are roughly the same at $f_T(\rho_C) = 210$ GHz. The drop in graphene is driven by the large reduction in g_m, from a peak of 14.9 mS/μm to a current-constrained 4.5 mS/μm, while the invariance in SL MoS_2 is due to a much smaller reduction in g_m, from a peak of 9 mS/μm to a current-constrained 6.9 mS/μm.

These results suggest that, when considering performance under the constraint of equal bias currents, as opposed to peak performance over all possible bias conditions, the gap in performance between graphene and SL MoS_2, for present-day contact technology, is not as severe as originally suggested in Section IV. In fact, with equal bias currents, a contact resistance of 375 $\Omega\cdot\mu$m realized in SL MoS_2 would be sufficient to bridge the gap to the value of unity-current-gain frequency currently possible in graphene.

3) THz Operation: For the bias current considered in this study, graphene cannot achieve an $f_T(\rho_C)$ of 1 THz; in fact, even with perfect graphene contacts, Fig. 7 shows that only $f_T(\rho_C) = 800$ GHz can be reached. On the other hand, for SL MoS_2, operation at 1 THz can be reached with a contact resistance of 80 $\Omega\cdot\mu$m, which is very nearly achieved with ML MoS_2.

4) Outlook with Perfect Contacts: Under equal bias currents, Fig. 7 shows that the 800-GHz value of $f_T(\rho_C)$ achievable with perfect graphene contacts can be matched by SL MoS_2 with 220 $\Omega\cdot\mu$m contacts.

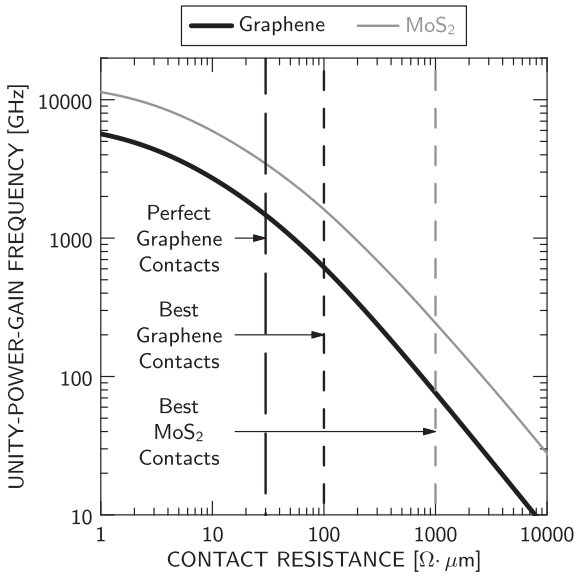

Fig. 9. Unity-power-gain frequency $f_{\max}(\rho_C)$ vs. the contact resistance ρ_C determining the source and drain contact resistances R_s and R_d, with R_g held at 1 Ω, and with the bias current constrained to 1.65 mA/μm.

C. Unity-Power-Gain Frequency $f_{\max}(\rho_C)$

Fig. 9 shows a plot of the unity-power-gain frequency $f_{\max}(\rho_C)$ vs. contact resistance ρ_C, found with a gate resistance $R_g = 1\,\Omega$, and *with the current constrained* to 1.65 mA/μm for both materials. The following observations can be made and should be contrasted with the results from Fig. 6, which showed the *peak* $f_{\max}(\rho_C)$ (over all bias conditions).

1) Comparison with Present-Day Contact Resistance: For graphene, at the present-day contact resistance of $\rho_C = 100\,\Omega \cdot \mu$m, the $f_{\max}(\rho_C)$ is reduced from a peak value of 1.1 THz in Fig. 6 to a current-constrained value of 600 GHz in Fig. 9. On the other hand, for SL MoS_2, at the present-day contact resistance of $\rho_C = 1\,\text{k}\Omega \cdot \mu$m, the value of 240 GHz from Fig. 6 remains nearly unaffected, reappearing in Fig. 9. As with the $f_T(\rho_C)$, a contact resistance of 375 $\Omega \cdot \mu$m in SL MoS_2 should be sufficient to match the 600-GHz value of $f_{\max}(\rho_C)$ possible in graphene.

2) THz Operation: With layout optimization to achieve minimum gate resistance, consistent with our assumption that $R_g = 1\,\Omega$, both materials should be able to achieve an $f_{\max}(\rho_C)$ of 1 THz under a constrained bias current, although neither can do so using currently achieved monolayer contact resistances. In graphene, ρ_C must be reduced to 50 $\Omega \cdot \mu$m (approaching perfect graphene contacts), and in SL MoS_2, ρ_C must be reduced to 170 $\Omega \cdot \mu$m (achieved so far only in ML MoS_2).

3) Outlook with Perfect Contacts: For graphene devices with perfect contacts ($\rho_C = 30\,\Omega \cdot \mu$m), a drop is observed from the peak $f_{\max}(\rho_C) = 3$ THz in Fig. 6 to the current-constrained value of $f_{\max}(\rho_C) = 1.5$ THz in Fig. 9. Section V concluded that the peak value of 3 THz would be impossible to reach using SL MoS_2 due to the small contact resistance required; however, the current-constrained $f_{\max}(\rho_C)$ of 1.5 THz in graphene could be reached by achieving $\rho_C = 110\,\Omega \cdot \mu$m in SL MoS_2, which has already been done with multi-layer structures.

D. Outcome

The most important outcome from Figs. 7 and 9 and the detailed discussion above is that MoS_2 becomes far more competitive under the condition of equal-current biasing. While graphene still retains its edge if the performance is compared using present-day contact resistances, the gap is substantially reduced, owing largely to the reduction in g_m that occurs in graphene once the current is constrained; SL MoS_2 can meet or exceed graphene's current-constrained benchmarks with contact resistances that have already been realized in multi-layer structures, including the possibility of operation at THz frequencies. We have illustrated this outcome using the technologically relevant current value of 1.65 mA/μm [38].

VII. Comparison With Experiment

While in general there have been many experimental studies of graphene and MoS_2 devices, the literature available with measured f_T and $f_{\max}$ is limited. For the purposes of comparison to experiment, we restrict our attention to the f_T, where sufficient experimental data is available to establish trends, and since f_T is far less sensitive to device layout in comparison to $f_{\max}$.

The current experiments on graphene and MoS_2 do not show the high values of f_T we discussed in Section IV for a device consistent with the 7-nm node, simply because the size of experimental structures has yet to shrink to the size of leading Si technology. Fig. 10 shows a summary of available experimental results of peak f_T vs. L_G for MoS_2 and graphene devices; for the purposes of the present comparison, where only trends are of interest, we need not distinguish between experimental values found from single- vs. multi-layer structures. We have superimposed our own single-layer simulation results on this graph.

Consider first the results for graphene. Since the majority of the graphene experimental f_T values have been achieved with a contact resistance on the order of 100 to 200 $\Omega \cdot \mu$m [10], [13], [63], we have added our simulated graphene f_T for a 7-nm node device, having a gate length of 12.7 nm, with an assumed contact resistance of 100 $\Omega \cdot \mu$m. Our simulation result shows good agreement with the trend line found from a linear regression against the graphene data, lending support to our approach and conclusions for graphene.

There is far less data available on the f_T for MoS_2, making it difficult to reliably extract a scaling trend. A starting point is a study [23] that included an examination of f_T vs. gate length; this work, in which $\rho_C = 2.5$ kΩ · μm, showed a strong $1/L_G$ scaling behavior for MoS_2 devices. The $1/L_G$ scaling behavior can be combined with the best experimental f_T values at a number of gate lengths, extracted from [22], [23], [64], to draw a trend line for MoS_2 in Fig. 10. The line is anchored at a point specified by an average of the experimental data, and it provides an idea of where the f_T values for MoS_2 devices should lie at shorter gate lengths, provided $\rho_C \sim 2.5\,\text{k}\Omega \cdot \mu$m,

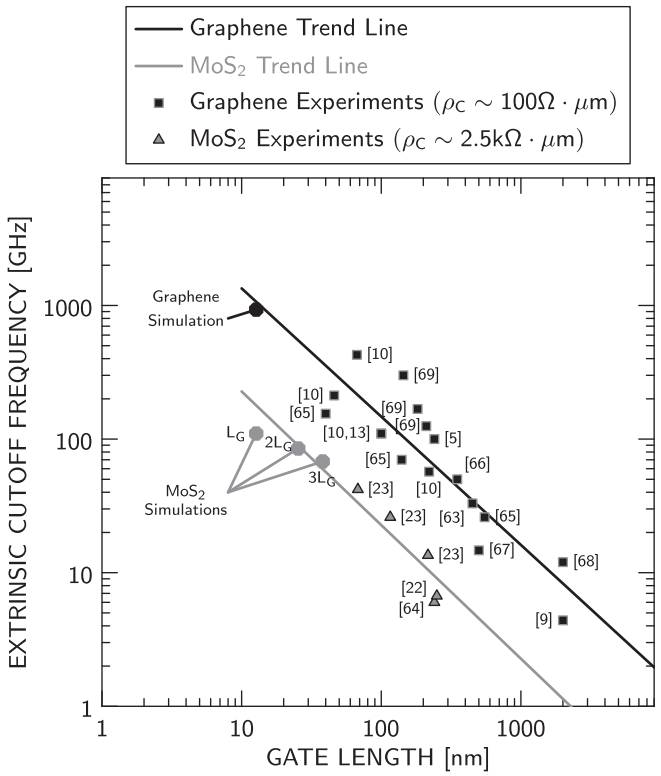

Fig. 10. Experimental data for peak f_T vs. gate length L_G for MoS_2 and graphene devices, with our simulation results superimposed. Experimental data for graphene is from [5], [9], [10], [13], [63], [65]–[69], and experimental data for MoS_2 is from [22], [23], [64]. The trend line for graphene applies for a contact resistance $\rho_C \sim 100\ \Omega \cdot \mu$m and that for MoS_2 applies for $\rho_C \sim 2.5\ \text{k}\Omega \cdot \mu$m, as discussed in the text.

the value used in all but one of the experiments; in that one experiment, ρ_C is slightly higher at 3.1 $\text{k}\Omega \cdot \mu$m, a detail that can be overlooked for the purpose of our comparison. We have additionally superimposed our simulation data for the f_T of MoS_2 devices at shorter gate lengths; in doing so, we chose $\rho_C = 2.5\ \text{k}\Omega \cdot \mu$m to be consistent with the experiments, and in addition to showing the result for $L_G = 12.7$ nm, applicable to the 7-nm ITRS node, we have added simulation data for the peak f_T at twice and three times this gate length. The simulation results are consistent with the experimental trend line, lending support to our approach and conclusions for MoS_2.

VIII. Conclusions

The following conclusions can be drawn from this comparison of the RF potential of graphene and SL MoS_2 transistors, using a device structure corresponding to the 7-nm technology node [38], with a focus on the impacts of the transconductance g_m and contact resistance ρ_C in determining the f_T and $f_{\max}$.

1) For equal bias voltages, graphene will always exhibit a higher g_m, which leads to a higher value of intrinsic $f_{\text{T,int}}$. For equal bias currents, the trend reverses, and SL MoS_2 gains the edge in g_m.
2) In terms of peak performance (over all bias conditions), SL MoS_2 lags graphene due to the relatively poor quality of SL MoS_2 contacts; for example, with current contact technology ($\rho_C = 100\,\Omega \cdot \mu$m in graphene and $\rho_C = 1\,\text{k}\Omega \cdot \mu$m in SL MoS_2), we observe $f_T = 930$ GHz and $f_{\max} = 1.1$ THz in graphene, but only $f_T = 230$ GHz and $f_{\max} = 260$ GHz in SL MoS_2. Considerable improvement in SL MoS_2 contacts is required for SL MoS_2 to bridge the gap, as we detailed in Sections IV and V.
3) In terms of the performance under the constraint of equal bias currents, set to the technologically relevant value of 1.65 mA/μm dictated by the ITRS [38], SL MoS_2 looks far more competitive, and SL MoS_2 can meet or exceed graphene's benchmarks by achieving contact resistances exhibited in experimental ML MoS_2 structures, as detailed in Section VI. SL MoS_2 gains ground on graphene when the current is constrained because its g_m remains less sensitive to bias conditions, whereas graphene requires large currents to sustain a large g_m.
4) The results are consistent with the trends established by experimental data for present-day devices, supporting the approach and conclusions.

Overall, our work shows that the peak performance edge will likely remain with graphene, due to lagging contact technology with SL MoS_2, but that SL MoS_2 can meet or exceed graphene in any application that constrains the bias current, provided only that SL MoS_2 can achieve contact resistances already realized in multi-layer structures. This result makes SL MoS_2 a highly attractive alternative to graphene for any application where the bias current is constrained (*e.g.*, to minimize power consumption), especially given that SL MoS_2 can also be used for digital logic, whereas graphene cannot.

Acknowledgment

The authors would like to thank Sam Anderson and Zhi Cheng (Jason) Yuan of the University of Alberta for their valuable feedback and suggestions.

References

[1] J. C. Slonczewski and P. R. Weiss, "Band structure of graphite," *Phys. Rev.*, vol. 109, no. 2, pp. 272–279, Jan. 1958.
[2] J.-H. Chen, C. Jang, S. Xiao, M. Ishigami, and M. S. Fuhrer, "Intrinsic and extrinsic performance limits of graphene devices on SiO_2," *Nature Nanotechnol.*, vol. 3, no. 4, pp. 206–209, Apr. 2008.
[3] J. Moser, A. Barreiro, and A. Bachtold, "Current-induced cleaning of graphene," *Appl. Phys. Lett.*, vol. 91, no. 16, Oct. 2007, Art. no. 163513.
[4] F. Schwierz, "Graphene transistors," *Nature Nanotechnol.*, vol. 5, no. 7, pp. 487–496, Jul. 2010.
[5] Y.-M. Lin *et al.*, "100-GHz transistors from wafer-scale epitaxial graphene," *Science*, vol. 327, p. 662, Feb. 2010.
[6] Z. Chen, Y.-M. Lin, M. J. Rooks, and P. Avouris, "Graphene nano-ribbon electronics," *Phys. E: Low-Dimensional Syst. Nanostruct.*, vol. 40, no. 2, pp. 228–232, Dec. 2007.
[7] Y. Zhang *et al.*, "Direct observation of a widely tunable bandgap in bilayer graphene," *Nature*, vol. 459, no. 7248, pp. 820–823, Jun. 2009.
[8] T. G. Pedersen, C. Flindt, J. Pedersen, N. A. Mortensen, A.-P. Jauho, and K. Pedersen, "Graphene antidot lattices: Designed defects and spin qubits," *Phys. Rev. Lett.*, vol. 100, no. 13, Apr. 2008, Art. no. 136804.
[9] J. S. Moon *et al.*, "Epitaxial-graphene RF field-effect transistors on Si-face 6H-SiC substrates," *IEEE Electron Device Lett.*, vol. 30, no. 6, pp. 650–652, Jun. 2009.
[10] R. Cheng *et al.*, "High-frequency self-aligned graphene transistors with transferred gate stacks," *Proc. Nat. Acad. Sci.*, vol. 109, no. 29, pp. 11588–11592, Jul. 2012.

[11] F. Schwierz, "Graphene transistors: Status, prospects, and problems," *Proc. IEEE*, vol. 101, no. 7, pp. 1567–1584, Jul. 2013.

[12] K. D. Holland, N. Paydavosi, N. Neophytou, D. Kienle, and M. Vaidyanathan, "RF performance limits and operating physics arising from the lack of a bandgap in graphene transistors," *IEEE Trans. Nanotechnol.*, vol. 12, no. 4, pp. 566–577, Jul. 2013.

[13] Z. Guo *et al.*, "Record maximum oscillation frequency in C-face epitaxial graphene transistors," *Nano Lett.*, vol. 13, no. 3, pp. 942–947, Mar. 2013.

[14] Y. Wu, D. B. Farmer, F. Xia, and P. Avouris, "Graphene electronics: Materials, devices, and circuits," *Proc. IEEE*, vol. 101, no. 7, pp. 1620–1637, Jul. 2013.

[15] H. Wang, A. Hsu, and T. Palacios, "Graphene electronics for RF applications," *IEEE Microw. Mag.*, vol. 13, no. 4, pp. 114–125, May 2012.

[16] S. Z. Butler *et al.*, "Progress, challenges, and opportunities in two-dimensional materials beyond graphene," *ACS Nano*, vol. 7, no. 4, pp. 2898–2926, Apr. 2013.

[17] C. Lee, X. Wei, J. W. Kysar, and J. Hone, "Measurement of the elastic properties and intrinsic strength of monolayer graphene," *Science*, vol. 321, no. 5887, pp. 385–388, Jul. 2008.

[18] S. Bertolazzi, J. Brivio, and A. Kis, "Stretching and breaking of ultrathin MoS_2," *ACS Nano*, vol. 5, no. 12, pp. 9703–9709, Dec. 2011.

[19] D. Akinwande, N. Petrone, and J. Hone, "Two-dimensional flexible nanoelectronics," *Nature Commun.*, vol. 5, Dec. 2014, Art. no. 5678.

[20] K. F. Mak, C. Lee, J. Hone, J. Shan, and T. F. Heinz, "Atomically thin MoS_2: A new direct-gap semiconductor," *Phys. Rev. Lett.*, vol. 105, no. 13, Sep. 2010, Art. no. 136805.

[21] R. Kappera *et al.*, "Phase-engineered low-resistance contacts for ultrathin MoS_2 transistors," *Nature Mater.*, vol. 13, no. 12, pp. 1128–1134, Dec. 2014.

[22] A. Sanne *et al.*, "Radio frequency transistors and circuits based on CVD MoS_2," *Nano Lett.*, vol. 15, no. 8, pp. 5039–5045, Aug. 2015.

[23] R. Cheng *et al.*, "Few-layer molybdenum disulfide transistors and circuits for high-speed flexible electronics," *Nature Commun.*, vol. 5, Oct. 2014, Art. no. 5143.

[24] G. Fiori *et al.*, "Electronics based on two-dimensional materials," *Nature Nanotechnol.*, vol. 9, no. 10, pp. 768–779, Oct. 2014.

[25] G. Fiori and G. Iannaccone, "Insights on radio frequency bilayer graphene FETs," in *IEEE Int. Electron Devices Meeting, San Francisco, CA, USA*, Dec. 2012, pp. 17.3.1–17.3.4.

[26] R. Grassi, T. Low, A. Gnudi, and G. Baccarani, "Contact-induced negative differential resistance in short-channel graphene FETs," *IEEE Trans. Electron Devices*, vol. 60, no. 1, pp. 140–146, Jan. 2013.

[27] W. S. Leong, X. Luo, Y. Li, K. H. Khoo, S. Y. Quek, and J. T. Thong, "Low resistance metal contacts to MoS_2 devices with nickel-etched-graphene electrodes," *ACS Nano*, vol. 9, no. 1, pp. 869–877, Jan. 2014.

[28] F. Xia, V. Perebeinos, Y.-M. Lin, Y. Wu, and P. Avouris, "The origins and limits of metal-graphene junction resistance," *Nature Nanotechnol.*, vol. 6, no. 3, pp. 179–184, Mar. 2011.

[29] J. T. Smith, A. D. Franklin, D. B. Farmer, and C. D. Dimitrakopoulos, "Reducing contact resistance in graphene devices through contact area patterning," *ACS Nano*, vol. 7, no. 4, pp. 3661–3667, Apr. 2013.

[30] S. Das, H.-Y. Chen, A. V. Penumatcha, and J. Appenzeller, "High performance multilayer MoS_2 transistors with scandium contacts," *Nano Lett.*, vol. 13, no. 1, pp. 100–105, Jan. 2013.

[31] J. Kang, W. Liu, and K. Banerjee, "High-performance MoS_2 transistors with low-resistance molybdenum contacts," *Appl. Phys. Lett.*, vol. 104, no. 9, Mar. 2014, Art. no. 093106.

[32] T. Roy *et al.*, "Field-effect transistors built from all two-dimensional material components," *ACS Nano*, vol. 8, no. 6, pp. 6259–6264, Jun. 2014.

[33] L. Yu *et al.*, "Graphene/MoS_2 hybrid technology for large-scale two-dimensional electronics," *Nano Lett.*, vol. 14, no. 6, pp. 3055–3063, Jun. 2014.

[34] L. Yang *et al.*, "High-performance MoS_2 field-effect transistors enabled by chloride doping: Record low contact resistance (0.5 $k\Omega \cdot \mu m$) and record high drain current (460 μ A/μm)," in *Proc. Symp. VLSI Technol. Dig. Tech. Papers*, Honolulu, HI, USA, Jun. 2014, pp. 1–2.

[35] A. A. Balandin, "Low-frequency $1/f$ noise in graphene devices," *Nature Nanotechnol.*, vol. 8, no. 8, pp. 549–555, Aug. 2013.

[36] S. L. Rumyantsev, C. Jiang, R. Samnakay, M. S. Shur, and A. A. Balandin, "$1/f$ noise characteristics of MoS_2 thin-film transistors: Comparison of single and multilayer structures," *IEEE Electron Device Lett.*, vol. 36, no. 5, pp. 517–519, May 2015.

[37] J. Renteria *et al.*, "Low-frequency $1/f$ noise in MoS_2 transistors: Relative contributions of the channel and contacts," *Appl. Phys. Lett.*, vol. 104, no. 15, Apr. 2014, Art. no. 153104.

[38] *The International Technology Roadmap for Semiconductors (ITRS)*. 2013. [Online]. Available: http://www.itrs.net/

[39] H. Fang *et al.*, "Degenerate n-doping of few-layer transition metal dichalcogenides by potassium," *Nano Lett.*, vol. 13, no. 5, pp. 1991–1995, May 2013.

[40] X. Wang *et al.*, "N-doping of graphene through electrothermal reactions with ammonia," *Science*, vol. 324, no. 5928, pp. 768–771, May 2009.

[41] Y. Liu *et al.*, "Towards barrier free contact to molybdenum disulfide using graphene electrodes," *Nano Lett.*, vol. 15, no. 5, pp. 3030–3034, May 2015.

[42] J. S. Moon *et al.*, "Ultra-low resistance ohmic contacts in graphene field effect transistors," *Appl. Phys. Lett.*, vol. 100, no. 20, May 2012, Art. no. 203512.

[43] S. Datta, "Nanoscale device modeling: the Greens function method," *Superlattices Microstruct.*, vol. 28, no. 4, pp. 253–278, Oct. 2000.

[44] A. S. Mayorov *et al.*, "Micrometer-scale ballistic transport in encapsulated graphene at room temperature," *Nano Lett.*, vol. 11, no. 6, pp. 2396–2399, Jun. 2011.

[45] K. Kaasbjerg, K. S. Thygesen, and K. W. Jacobsen, "Phonon-limited mobility in n-type single-layer MoS_2 from first principles," *Phys. Rev. B*, vol. 85, no. 11, Mar. 2012, Art. no. 115317.

[46] X. Li, J. T. Mullen, Z. Jin, K. M. Borysenko, M. B. Nardelli, and K. W. Kim, "Intrinsic electrical transport properties of monolayer silicene and MoS_2 from first principles," *Phys. Rev. B*, vol. 87, no. 11, Mar. 2013, Art. no. 115418.

[47] L. Liu, Y. Lu, and J. Guo, "On monolayer MoS_2 field-effect transistors at the scaling limit," *IEEE Trans. Electron Devices*, vol. 60, no. 12, pp. 4133–4139, Dec. 2013.

[48] H. Peelaers and C. G. Van de Walle, "Effects of strain on band structure and effective masses in MoS_2," *Phys. Rev. B*, vol. 86, no. 24, Dec. 2012, Art. no. 241401.

[49] R. Venugopal, Z. Ren, S. Datta, M. Lundstrom, and D. Jovanovic, "Simulating quantum transport in nanoscale transistors: Real versus mode-space approaches," *J. Appl. Phys.*, vol. 92, no. 7, pp. 3730–3739, Oct. 2002.

[50] S. Datta, *Electronic Transport in Mesoscopic Systems*, 1st ed. New York, NY, USA: Cambridge Univ. Press, 1997.

[51] M. P. L. Sancho, J. M. L. Sancho, J. M. L. Sancho, and J. Rubio, "Highly convergent schemes for the calculation of bulk and surface Green functions," *J. Phys. F, Metal Phys.*, vol. 15, no. 4, pp. 851–858, Apr. 1985.

[52] A. Svizhenko, M. P. Anantram, T. R. Govindan, B. Biegel, and R. Venugopal, "Two-dimensional quantum mechanical modeling of nanotransistors," *J. Appl. Phys.*, vol. 91, no. 4, pp. 2343–2354, Feb. 2002.

[53] *Comsol Multiphysics, COMSOL Inc., Stockholm, Sweden*, 2013.

[54] K. L. Grosse, M.-H. Bae, F. Lian, E. Pop, and W. P. King, "Nanoscale joule heating, peltier cooling and current crowding at graphene-metal contacts," *Nature Nanotechnol.*, vol. 6, no. 5, pp. 287–290, May 2011.

[55] K. Nagashio, T. Nishimura, K. Kita, and A. Toriumi, "Contact resistivity and current flow path at metal/graphene contact," *Appl. Phys. Lett.*, vol. 97, no. 14, Oct. 2010, Art. no. 143514.

[56] H. Liu *et al.*, "Statistical study of deep submicron dual-gated field-effect transistors on monolayer chemical vapor deposition molybdenum disulfide films," *Nano Lett.*, vol. 13, no. 6, pp. 2640–2646, Jun. 2013.

[57] J. Jimenez Tejada, J. Lopez Villanueva, P. Lopez Varo, K. Awawdeh, and M. Jamal Deen, "Compact modeling and contact effects in thin film transistors," *IEEE Trans. Electron Devices*, vol. 61, no. 2, pp. 266–277, Feb. 2014.

[58] H. Liu *et al.*, "Switching mechanism in single-layer molybdenum disulfide transistors: an insight into current flow across Schottky barriers," *ACS Nano*, vol. 8, no. 1, pp. 1031–1038, Jan. 2013.

[59] Y. Guo *et al.*, "Study on the resistance distribution at the contact between molybdenum disulfide and metals," *ACS Nano*, vol. 8, no. 8, pp. 7771–7779, Aug. 2014.

[60] K. Ganapathi, Y. Yoon, M. Lundstrom, and S. Salahuddin, "Ballistic I-V characteristics of short-channel graphene field-effect transistors: Analysis and optimization for analog and RF applications," *IEEE Trans. Electron Devices*, vol. 60, no. 3, pp. 958–964, Mar. 2013.

[61] T. C. Lim and G. A. Armstrong, "The impact of the intrinsic and extrinsic resistances of double gate SOI on RF performance," *Solid-State Electron.*, vol. 50, no. 5, pp. 774–783, May 2006.

[62] S. Mason, "Power gain in feedback amplifier," *Trans. IRE Prof. Group Circuit Theory*, vol. 1, no. 2, pp. 20–25, Jun. 1954.

[63] H. Wang *et al.*, "BN/graphene/BN transistors for RF applications," *IEEE Electron Device Lett.*, vol. 32, no. 9, pp. 1209–1211, Sep. 2011.
[64] D. Krasnozhon, D. Lembke, C. Nyffeler, Y. Leblebici, and A. Kis, "MoS_2 transistors operating at gigahertz frequencies," *Nano Lett.*, vol. 14, no. 10, pp. 5905–5911, Oct. 2014.
[65] Y. Wu *et al.*, "High-frequency, scaled graphene transistors on diamond-like carbon," *Nature*, vol. 472, no. 7341, pp. 74–78, Apr. 2011.
[66] Y.-M. Lin, H.-Y. Chiu, K. A. Jenkins, D. B. Farmer, P. Avouris, and A. Valdes-Garcia, "Dual-gate graphene FETs with f_t of 50 GHz," *IEEE Electron Device Lett.*, vol. 31, no. 1, pp. 68–70, Jan. 2010.
[67] I. Meric, N. Baklitskaya, P. Kim, and K. L. Shepard, "RF performance of top-gated, zero-bandgap graphene field-effect transistors," in *Proc. IEEE Int. Electron Devices Meeting*, San Francisco, CA, USA, Dec. 2008, pp. 1–4.
[68] A. Hsu, H. Wang, K. K. Kim, J. Kong, and T. Palacios, "Impact of graphene interface quality on contact resistance and RF device performance," *IEEE Electron Device Lett.*, vol. 32, no. 8, pp. 1008–1010, Aug. 2011.
[69] L. Liao *et al.*, "High-speed graphene transistors with a self-aligned nanowire gate," *Nature*, vol. 467, pp. 305–308, Sep. 2010.

Kyle D. Holland received the B.Sc. degree in engineering physics (nanoengineering option) in 2009 from the University of Alberta, Edmonton, AB, Canada, where he is currently working toward the Ph.D. degree in electrical engineering.

His research interests include the quantum simulation of carbon-based nanoelectronics, with an emphasis on modeling the high-frequency performance of graphene devices.

Ahsan U. Alam received the Ph.D. degree in electrical engineering from the University of Alberta, Edmonton, AB, Canada, in 2015.

He is currently an Applications Engineer at Lumerical Solutions, Inc., Vancouver, BC, Canada. His research interests include the modeling and simulation of micro- and nanoscale electronic and optoelectronic devices for current and future technologies.

Navid Paydavosi received the Ph.D. degree in electrical engineering from the University of Alberta, Edmonton, AB, Canada, in 2011.

He worked for the BSIM Group at the University of California, Berkeley, as a Postdoctoral Scholar from 2012 to 2014. He has published several research papers on the theory and modeling of modern Si-MOSFETs and its future alternatives, including carbon-based and III–V high-electron mobility devices. He is currently a Device Engineer with Intel Corp., Hillsboro, OR, USA, working on process technology development for advanced technology nodes.

Michael Wong received the B.Sc. degree in computer engineering from the University of Alberta, Edmonton, AB, Canada, in 2013, where he is currently working toward the Ph.D. degree in electrical engineering.

His current research interests include the modeling and simulation of nanoscale devices, including FinFETs and 2-D FETs.

Christopher M. Rogers received the B.Sc. degree in engineering physics from the University of Alberta, Edmonton, AB, Canada, in 2012, and the M.Sc. degree in electrical engineering in 2015 from Stanford University, Stanford, CA, USA, where he is currently working toward the Ph.D. degree in electrical engineering in the group of H. Mabuchi.

His current research interests broadly span nonlinear optics, quantum optics, and optical information processing. More specifically, he is interested in fabricating nonlinear optical devices using 2-D materials, and as well as fabricating chip-based optical parametric oscillators.

Shahriar Rizwan received the B.Sc. degree in electrical and electronic engineering from Bangladesh University of Engineering and Technology, Dhaka, Bangladesh, in 2012. He is currently working toward the Ph.D. degree in electrical engineering with the University of Alberta, Edmonton, AB, Canada.

He was a Software Engineer with the Samsung R&D Institute Bangladesh, Dhaka, from 2012 to 2014.

Diego Kienle received the Ph.D. degree in theoretical physics from the Research Center Juelich and the University Saarland, Saarbrücken, Germany.

After appointments at Purdue University and Sandia National Laboratories, he is currently with the Institute of Theoretical Physics, University of Bayreuth, Bayreuth, Germany. His research interests include the theory and simulation of quantum kinetic transport in nanoscale materials and devices.

Mani Vaidyanathan received the Ph.D. degree in electrical engineering from the University of British Columbia, Vancouver, BC, Canada.

He is currently an Associate Professor with the Department of Electrical and Computer Engineering, University of Alberta, Edmonton, AB, Canada. His research interests include the modeling, simulation, and understanding of electronic devices for future electronics, with a present focus on the radio-frequency performance of FinFETs and 2-D materials.